Inorganic Chemistry

pubs.acs.org/IC

Article

Direct Mechanochemical Synthesis, Phase Stability, and Electrochemical Performance of α-$NaFeO_2$

Rebecca D. McAuliffe, Gabrielle E. Kamm, Matthew J. McDermott, Raphaël P. Hermann, Neyanel Vasquez-Garcia, Robert L. Sacci, Kristin A. Persson, Karena W. Chapman, and Gabriel M. Veith*

Cite This: https://doi.org/10.1021/acs.inorgchem.2c03286

Read Online

ACCESS | Metrics & More | Article Recommendations | Supporting Information

ABSTRACT: To better understand polymorph control in transition metal oxides, the mechanochemical synthesis of $NaFeO_2$ was explored. Herein, we report the direct synthesis of α-$NaFeO_2$ through a mechanochemical process. By milling Na_2O_2 and γ-Fe_2O_3 for 5 h, α-$NaFeO_2$ was prepared without high-temperature annealing needed in other synthesis methods. While investigating the mechanochemical synthesis, it was observed that changing the starting precursors and mass of precursors affects the resulting $NaFeO_2$ structure. Density functional theory calculations on the phase stability of $NaFeO_2$ phases show that the α phase is stabilized over the β phase in oxidizing environments, which is provided by the oxygen-rich reaction between Na_2O_2 and Fe_2O_3. This provides a possible route to understanding polymorph control in $NaFeO_2$. Annealing the as-milled α-$NaFeO_2$ at 700 °C has resulted in increased crystallinity and structural changes that improved electrochemical performance in terms of capacity over the as-milled sample.

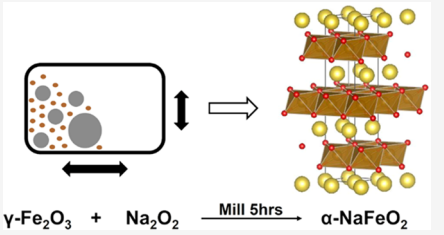

1. INTRODUCTION

The controlled synthesis of layered transition metal oxides (AMO_2, where A is an alkali metal and M is a transition metal) is one of the most critical aspects of the development of battery materials. Candidate compounds include $LiCoO_2$ and related compounds containing Ni, Mn, Fe, Al, and other transition metals,[1−8] as well as their sodium analogs.[9−19] There are numerous methods reported to fabricate these layered metal oxides, including direct solid-state synthesis,[6,7,16−22] hydrothermal,[23] molten salts,[10,24−26] precipitation,[1,2,27−30] and vapor deposition among other methods.[3−5,31−33] Each of these synthesis techniques imparts unique morphologies, sizes, as well as transition-metal ordering within the crystal lattice that mediates electrode fabrication and electrochemical performance.[26,29,30,33−36]

One such cathode material is α-$NaFeO_2$, also known as O3-type $NaFeO_2$ due to its stacking, which has a layered rock-salt structure (Figure 1a) that provides routes for Na-ion mobility.[37] With an operating voltage of 3.3 V vs Na/Na^+ and its high earth abundance, α-$NaFeO_2$ is a promising cathode material for sodium-ion batteries.[38] α-$NaFeO_2$ is commonly synthesized by mixing a Na-containing precursor (Na_2CO_3, NaOH, Na_2O_2) with iron oxide (α-Fe_2O_3, γ-Fe_2O_3, Fe_3O_4) and heating the sample between 400 and 700 °C.[38−45] However, care must be taken to select the correct precursors and synthesis conditions; several different polymorphs of $NaFeO_2$ exist (Figure 1) and, often, a mixture of both α- and β-$NaFeO_2$ (wurtzite-like structure) is formed during synthesis.[42]

Here, we report the direct synthesis of α-$NaFeO_2$ by mechanochemical milling of Na_2O_2 and γ-Fe_2O_3. In our procedure, α-$NaFeO_2$ is synthesized without any additional heat treatments. While many cathode materials have been synthesized by mechanochemical methods, in this study, we performed density functional theory (DFT) calculations to understand the stability of α- and β-$NaFeO_2$ and discuss the role of charged point defects (especially vacancies) in preferentially stabilizing the α phase over the other known $NaFeO_2$ polymorphs in oxygen-rich environments.[46−48] Upon annealing the as-milled material, we obtained a sample with larger particle sizes, higher crystallinity, and improved electrochemical properties.

2. METHODS

2.1. Experimental Methods. α-$NaFeO_2$ was synthesized by first combining Na_2O_2 (Sigma-Aldrich) and γ-Fe_2O_3 (Inframat Advanced Materials) into a 65 mL stainless-steel SPEX jar with six 5 mm and three 1/2-in. stainless-steel milling media in an Ar-filled glovebox. Na_2O_2 and γ-Fe_2O_3 (1:1 molar ratio) were milled under Ar for 5 h using a SPEX 8000M mixer/mill. The resulting powder was then heated in air to 700 °C for 12 h at a 10 °C/min heating rate. After

Received: September 15, 2022

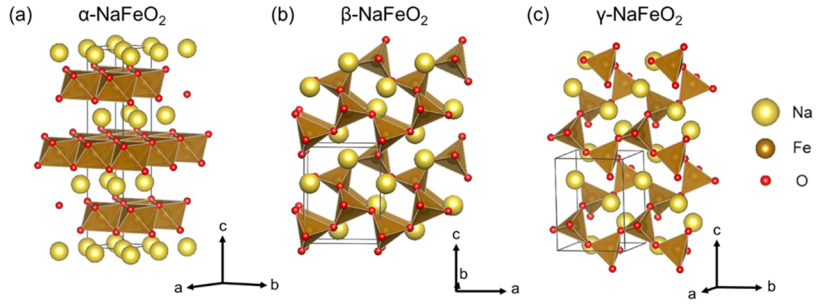

Figure 1. Polymorphs of $NaFeO_2$. (a) α-$NaFeO_2$ (R-3m) has a layered structure with Na ions between FeO_2 layers. (b) β-$NaFeO_2$ ($Pna2_1$) has a wurtzite-like structure with corner-shared Fe tetrahedra and (c) γ-$NaFeO_2$ ($P2_12_12_1$) is a high-temperature phase similar to β-$NaFeO_2$, with orthorhombic symmetry. The black outline represents the unit cell of each structure.

heating for 12 h, the sample was furnace-cooled by turning off the heating of the furnace with no specific cooling rate set. A synthesis graph of this synthesis process generated using SynCheck is shown in Figure S1.[49] Na_2O_2 is a reactive chemical. It is a strong oxidizer, an explosion hazard, and water-reactive. All preparation and reactions were performed under Ar, ensuring that no water, metal powders, or organic compounds were present in a milling jar during the reaction.

Data suitable for X-ray diffraction and PDF analyses were collected at 28-ID-1, at the National Synchrotron Light Source II, Brookhaven National Laboratory (λ = 0.1665 Å). The distance between the sample and detector was calibrated using a CeO_2 standard (NIST SRM 674b) and GSAS II.[50] Rietveld refinements were carried out in a TOPAS-Academic v6.[51] Extraction of PDF data was done in xPDF Suite, and modeling of the PDF data was done in PDFgui.[51,52] Details of the refinements can be found in Section S5. Bond lengths of interest were quantified by fitting Gaussian functions to the peaks in the PDF data within fityk.[53] Crystal structures were visualized using VESTA.[54]

Scanning electron microscopy (SEM) was performed using a Hitachi TM3030 Plus.

Samples were prepared for Mössbauer spectroscopy by mixing 35 mg of $NaFeO_2$ powders with BN inside of an Ar-filled glovebox and placing the materials in a 12.5 mm diameter hole of a Ti sample holder to disperse and minimize absorption of the sample. The samples were sealed using Kapton tape and contained in a heat-sealed polyethylene bag to prevent any reaction with moisture and air during the measurement; a second set of measurements was carried out on samples exposed under ambient conditions for 2 weeks. Mössbauer spectra were measured at room temperature using a 1 mCi cobalt-57@Rh source and a krypton gas-proportional counter in the ±8 mm/s range for the sealed samples and ±4 mm/s range for the ambient condition samples. The Wissel constant acceleration drive was calibrated using the α-Fe spectrum; isomer shifts are relative to α-Fe.[55,56]

For inductively coupled plasma−optical emission spectroscopy (ICP-OES) chemical analysis, 18 MW ultrapure deionized water, HCl acid (Aristar Plus, VWR Chemicals), and HNO_3 acid (Aristar Plus, VWR Chemicals) were used as reagents. A mixture of HCl/HNO_3 was prepared in a 3:1 volume ratio to dissolve $NaFeO_2$. ICP standards (1000 mg/L) were purchased from Sigma-Aldrich (TraceCERT grade) and diluted to prepare standards. ICP-OES measurements were carried out on a Thermo Scientific iCAP 7400 ICP-OES Duo and iCAP 7600 (Thermo Fisher Scientific).

Composite electrodes were fabricated using $NaFeO_2$/C45 Carbon Black (Timcal)/PVDF Kureha Cathode Grade in an 80/10/10 weight ratio. The cathode and C45 were dry mixed using a vortex mixer, followed by the addition of a premade solution of PVDF dissolved in N-methyl-2-pyrrolidone (Aldrich—anhydrous 99.5%). The mixture was blended using seven 5 mm yttria-stabilized ZrO_2 spherical media and a Turbula for 1 h. The material was cast with an areal density of 1 mAh/cm^2 on a battery-grade aluminum foil and dried at 120 °C under static vacuum for 15 h prior to transfer into an argon-filled glovebox. Half-cells were built using a 1 M $NaPF_6$ (STELLA, Singapore, 98%, dried at 110 °C in vacuum)/propylene carbonate electrolyte (Aldrich 99.7% and further dried over 3A zeolite sieves). The sodium counter electrode was made from a sodium dry stick (Aldrich). The oxide coating was removed, and the sodium was pressed and rolled into a ≤1 mm thick foil between two pieces of polypropylene and then punched into an 18 mm disk. The cell was assembled in a coin cell (2325, Pred Materials) using 40 μL of electrolyte and a Dreamweaver Gold 40 separator. Electrodes were cycled at a rate of C/5 using a MACCOR battery cycler in constant current/constant voltage mode (C/5; C/10) at 25 °C.

2.2. Computational Methods. Density functional theory (DFT) calculations were performed using the Vienna Ab initio Simulation Package (VASP, v6.2.1) with projector augmented wave (PAW) pseudopotentials.[57,58] All relaxation calculations were performed with the Perdew−Burke−Ernzerhof (PBE) exchange−correlation functional[59] within the generalized gradient approximation with Hubbard U (GGA + U) using a plane-wave cutoff energy of 520 eV. A value of U = 5.3 eV was used for Fe, as determined via the approach from Wang et al.[60] and implemented in pymatgen.[61] The HSE06 exchange−correlation functional[62] was used for the calculation of band structures used in point defect corrections.

The α-, β-, and γ-$NaFeO_2$ structures were originally acquired from the Materials Project database[63] with identifiers mp-19359, mp-21060, and mp-21880, respectively. Collinear magnetic orderings were determined for each structure via the magnetic ordering workflow developed by Horton et al.[64] and implemented in atomate.[65]

Point defect formation energies were calculated using a charged defect supercell approach with finite-size corrections developed by Freysoldt et al.[66] and implemented by Broberg et al.[67] Only charged vacancies were considered in our analysis. We included all integer charge states in the ranges Na: [−1, 1], Fe: [−4, 4], and O: [−2, 2]. Vacancy sites were identified using pymatgen, and all supercell structures were constructed with a scaling of 3 × 2 × 2, resulting in a total size of 192 atoms for each calculation. Each defected structure was initialized with its corresponding magnetic ordering, as identified via the aforementioned workflow.

The Na−Fe−O chemical potential diagram was constructed using thermodynamic data acquired from the Materials Project (v2021.11.10) via the approach described by Todd et al.[68] and implemented in pymatgen.[61] The relative stability of the bulk phases and their regions of stability on the chemical potential diagram were calculated at T = 0 K (i.e., without finite-temperature effects). The chemical potentials have not been re-referenced and are plotted with respect to the energy output from the VASP calculations.

The thermodynamic stability of $NaFeO_2$ polymorphs as a function of environmental chemical potentials was determined by identifying the polymorph with the minimum Gibbs free energy (including the contribution from equilibrium defect concentrations) at each set of chemical potentials within the stability domain of the bulk $NaFeO_2$ phase on the chemical potential diagram. The Gibbs free energy, G, of each phase was calculated as

$$G(P, T) = G_{\text{bulk}}(P, T) - k_B T \sum_i c_i^{\text{eq}}(P, T) \quad (1)$$

https://doi.org/10.1021/acs.inorgchem.2c03286
Inorg. Chem. XXXX, XXX, XXX−XXX

where G_{bulk} is the Gibbs free energy of the bulk $NaFeO_2$ phase, P is the pressure, T is the temperature, k_B is the Boltzmann's constant, and c_i^{eq} is the equilibrium defect molar concentration for a defect indexed i. This formula accounts for the total free energy decrease from all point defects at their equilibrium concentrations (i.e., where $dG/dc_i = 0$).[69] We approximated the Gibbs free energy of the bulk phase as $G_{bulk} \approx E_{bulk}$; i.e., assuming minimal contributions from the bulk mechanical (PV) and bulk entropic (TS) terms. A temperature of T = 1000 K (slightly above the annealing temperature of 700 °C) was used in eq 1 and in the self-consistent solution of the Fermi energy, E_F, that enters the calculation of equilibrium defect concentrations. The Fermi energy was solved in a self-consistent fashion at each set of chemical potentials within the bounds of the $NaFeO_2$ stability region on the Na−Fe−O chemical potential diagram. This resulted in changes in the vacancy formation energies and thus equilibrium concentrations as a function of chemical potentials.

3. RESULTS AND DISCUSSION

3.1. Mechanochemical Synthesis of α-$NaFeO_2$. α-$NaFeO_2$ was synthesized through a mechanochemical process without external heating. The selection of a Fe_2O_3 precursor polymorph and the amount of milled material were critical to polymorphic control.

The Fe_2O_3 precursor selected played a role in the resulting $NaFeO_2$ product that was synthesized. Reactions between Na_2O_2 and α-Fe_2O_3 resulted in a mixture of α- and β-$NaFeO_2$, while for the same conditions, reactions between Na_2O_2 and γ-Fe_2O_3 resulted in pure α-$NaFeO_2$. The X-ray diffraction (XRD) results from these mechanochemical reactions are shown in Figure S2. As previously reported by Takeda et al., the formation of β-$NaFeO_2$ from α-Fe_2O_3 and α-$NaFeO_2$ from γ-Fe_2O_3 is likely due to the similarity in the oxygen packing in the structure of the starting materials as both β-$NaFeO_2$ and α-Fe_2O_3 have hexagonal closest packing (hcp) of oxygen, and α-$NaFeO_2$ and γ-Fe_2O_3 have cubic closest packing (ccp) of oxygen.[42] However, the results obtained from this mechanochemical synthesis differ from the solid-state reactions that have been previously reported. In the solid-state reactions, both α-Fe_2O_3 and γ-Fe_2O_3 will form α-$NaFeO_2$ when reacted with Na_2O_2 above 400 °C.[42] It is shown that in solid-state reactions with α-Fe_2O_3, β-$NaFeO_2$ forms as an intermediate phase, which proceeds to transform into α-$NaFeO_2$ at 400°C.[42] However, even with heating the sample to 700 °C for 12 h, pure α-$NaFeO_2$ is not obtained *via* the mechanochemical synthesis using α-Fe_2O_3. Mechanochemical reactions with γ-Fe_2O_3, however, form α-$NaFeO_2$ without any additional heating required. In solid-state reactions between γ-Fe_2O_3 and Na-containing precursors, γ-Fe_2O_3 is known to form a Na-doped γ-Fe_2O_3 structure before reacting fully to form α-$NaFeO_2$.[42] This intermediate Na-doped γ-Fe_2O_3 structure was not observed in this study, but the formation of this intermediate may be present at shorter milling times that were not investigated here.

The amount of material being milled under the same milling conditions is also important. When milling up to 2.25 g of the combined precursors (γ-Fe_2O_3 and Na_2O_2), the synthesis proceeded as predicted forming pure α-$NaFeO_2$; however, when the amount of precursor being milled was increased to 5 g, the synthesis formed a mixture of α- and β-$NaFeO_2$. The refinements of X-ray diffraction data for these experiments are shown in Figure S3.

The change in polymorph formation as a function of initial precursor mass could be due to several different possibilities. First, during the synthesis of α-$NaFeO_2$, a Na-doped γ-Fe_2O_3 phase forms, which stabilizes γ-Fe_2O_3.[42] Without this sodiation step, γ-Fe_2O_3 will transform into α-Fe_2O_3 at 400 °C. It is possible that with the additional material present, either less mixing occurs or the sample heating is altered, leading to less doping into γ-Fe_2O_3. Therefore, upon local heating during milling, α-Fe_2O_3 is formed, which will react with Na_2O_2 to form β-$NaFeO_2$. Second, it is also possible that the formation of O_2 is limiting the sodiation of γ-Fe_2O_3. As the mass of precursors is increased, the amount of gas evolved from the precursors increases as well. Indeed, the sodiation of γ-Fe_2O_3 is slower when reacting with $NaNO_3$ and γ-Fe_2O_3 in an atmosphere of O_2 rather than N_2.[41] These results show that reaction environment and defect formation could play a large role in directing the synthesis of a specific polymorph. Understanding the role of defects and environmental conditions is critical to understanding how to directly synthesize in this system and for other layered transition metal oxides.

3.2. Phase Stability of $NaFeO_2$ Polymorphs. To better understand how synthesis conditions influence polymorph selection in $NaFeO_2$, charged point defect calculations were performed with density functional theory (DFT) on the three known $NaFeO_2$ structures: α, β, and γ. To acquire the input structures, we first performed collinear magnetic ordering analysis and reoptimized the three $NaFeO_2$ polymorph structures originally obtained from the Materials Project (see Section 2.2). The ground-state magnetic orderings are illustrated in Figure S4. The calculated properties of these re-relaxed structures are shown in Table 1.

Table 1. Calculated Properties of $NaFeO_2$ Polymorph Structures

structure	space group	magnetic ordering	bandgap (eV)	stability (meV/atom)
α	$R\text{-}3m$	AFM	2.65	+8.7
β	$Pna2_1$	AFM	3.32	+0 (stable)
γ	$P2_12_12_1$	AFM	3.21	+7.6

With the acquired antiferromagnetic (AFM) orderings, β-$NaFeO_2$ is predicted to be stable from the DFT calculations using the GGA + U level of theory. The γ phase is predicted to be the next most stable with an energy of 7.6 meV/atom above that of the ground-state (β) phase, followed by the α phase with an energy difference of +8.7 meV/atom above the ground state. The lowest energy AFM magnetic ordering was necessary for both correctly identifying this polymorph ordering and for converging the defect calculations, as we discussed in a previous work.[70]

The defect calculations reveal that the α-$NaFeO_2$ phase, which is nominally metastable, may be stabilized in oxygen-rich environments, i.e., where the oxygen chemical potential, μ_O, is high. The calculated vacancy formation energy diagrams for each of the $NaFeO_2$ polymorphs are plotted in Figure 2. These defect formation energy diagrams show the energy cost to form a vacancy in each of the structures as a function of the Fermi energy, which, in a semiconductor/insulator, is bounded by the band gap of the material (dashed vertical lines). The changing slope of each curve in the diagram indicates a vacancy of a different charge state. Only the charge state with the minimum energy is shown. Note that the defect formation energy diagram for β-$NaFeO_2$ (Figure 2b) contains two unique

https://doi.org/10.1021/acs.inorgchem.2c03286
Inorg. Chem. XXXX, XXX, XXX−XXX

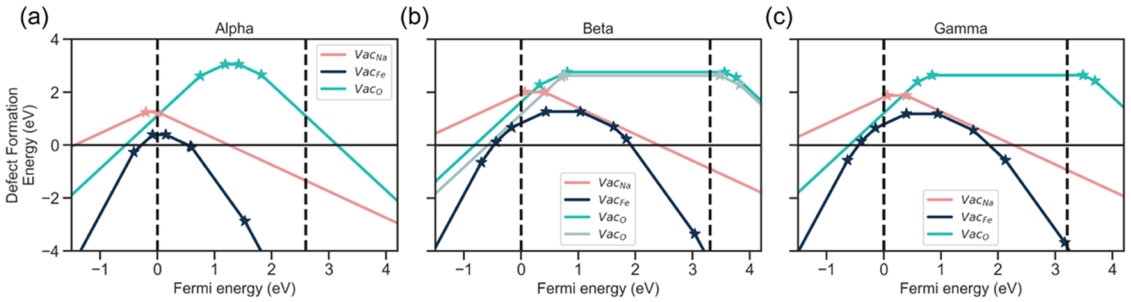

Figure 2. Calculated defect formation energies and charge-state transitions as a function of Fermi energy for vacancies in the (a) α, (b) β, and (c) γ of $NaFeO_2$. The defect formation energy curves shown are calculated at chemical potentials corresponding to where $NaFeO_2$ is thermodynamically stable with Na_4FeO_4 and Na_3FeO_3, near where α-$NaFeO_2$ is predicted to be stabilized over the β phase (i.e., $\mu_{Na} = -3.28$ eV, $\mu_{Fe} = -12.10$ eV, and $\mu_O = -5.76$ eV).

oxygen vacancy curves, as there are two symmetrically distinct oxygen vacancy sites in this polymorph.

While β- and γ-$NaFeO_2$ have very similar formation energy curves, it is apparent that α-$NaFeO_2$ has noticeably lower stability of the neutral oxygen vacancy charge state and consistently lower formation energies for cation vacancies (both Fe and Na). Indeed, as one varies the applied chemical potentials toward regions of higher μ_O (and correspondingly lower μ_{Fe} and μ_{Na}), the self-consistent solution of the Fermi energy for the α phase leads to low values ($E_F \rightarrow 0$), where Fe vacancies have a charge state of zero. When this is coupled with the low values of μ_{Fe} in this region, the result is a significant decrease in the formation energy of Fe vacancies ($\Delta E_F \rightarrow 0$) and thus, a corresponding increase in the predicted equilibrium concentration of these defects. Hence, we find a defect-dependent phase transition, where α-$NaFeO_2$ is stabilized by defect accommodation, as illustrated in the chemical potential diagram in Figure 3. This phase transition is predicted to become favorable near the three-phase point, where $NaFeO_2$ is in thermodynamic equilibrium with Na_4FeO_4 and Na_3FeO_3. The α-phase remains stable over the competing β and γ phases throughout the high-oxygen chemical potential region.

We have noted via changes in color shading in Figure 3, where the predicted equilibrium molar defect concentrations rapidly increase to high concentrations (>10%), well above the typical "dilute limit" assumed in point defect calculations. Plots of equilibrium defect concentrations as a function of chemical potentials are shown in Figure S5. It should be expected that the defect−defect interactions will begin to occur before a 10% molar concentration is reached, the effects of which are not captured by our computational approach. However, the presence of a predicted transition from β- to α-$NaFeO_2$ should not be affected.

Interestingly, the γ-$NaFeO_2$ phase is not predicted to be stable over any set of chemical potentials. While the energy of the γ phase is predicted to be lower than that of the α-phase, it has very similar defect formation energy curves to β-$NaFeO_2$, which means that it follows the same trends in Gibbs free energy as a function of chemical potentials (see Figure S6). Even when β-$NaFeO_2$ is predicted to further stabilize at the low oxygen chemical potentials (near the Fe/$NaFeO_2$ boundary in Figure 3), the free energy of the γ-phase remains consistently higher.

The exact set of chemical potentials at which the $\beta \rightarrow \alpha$ phase transition is expected to occur is likely sensitive to small errors in calculations, including our assumption that differences

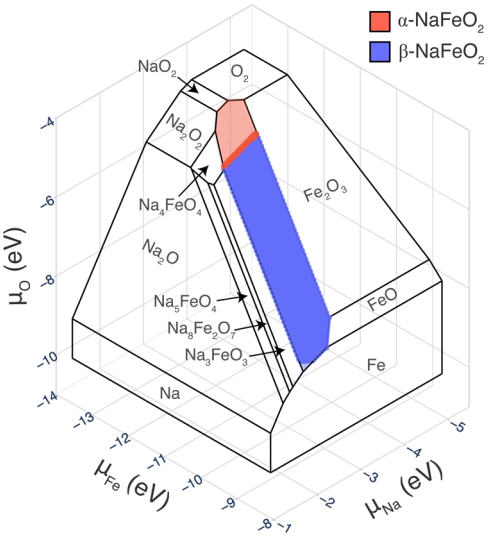

Figure 3. Defect-dependent stability phase diagram of $NaFeO_2$ polymorphs from density functional theory calculations. The stability of the α, β, and γ polymorphs is compared as a function of elemental chemical potentials on the Na−Fe−O chemical potential diagram. Color shading indicates the stable polymorph at each point on the chemical potential diagram surface, bounded by the stability of the $NaFeO_2$ bulk composition. The γ phase is not predicted to be stable at any set of chemical potentials and hence does not appear on the diagram. Lighter shading denotes regions, where at least one defect exceeds 10% molar concentration (i.e., well above the dilute limit assumed in point defect calculation methodology).

in finite-temperature effects are negligible for both the free energies of each bulk phase as well as individual defect energies. We also did not model other intrinsic point defects (e.g., interstitials and substitutions), which may contribute to defect-dependent stabilization. However, the presence of a phase transition dependent on the oxygen chemical potential is meaningful and supported by experimental observations of $NaFeO_2$ synthesis. For example, Na_2O_2 is often used as a precursor (instead of Na_2O) for solid-state synthesis of $NaFeO_2$, despite having a much less favorable reaction energy ($\Delta E_{rxn} = -0.073$ eV/atom for Na_2O_2 vs -0.196 eV/atom for Na_2O).[7,42] Furthermore, the use of Na_2O_2 will result in the production of O_2 gas via the balanced reaction $Na_2O_2 + Fe_2O_3 \rightarrow 2NaFeO_2 + 0.5O_2$, which may produce a locally oxidizing environment during synthesis, especially when performed in a sealed container. Finally, it has been suggested that the phase transition from α-$NaFeO_2 \rightarrow \beta$-$NaFeO_2$ occurs at 760 °C.[71]

https://doi.org/10.1021/acs.inorgchem.2c03286
Inorg. Chem. XXXX, XXX, XXX−XXX

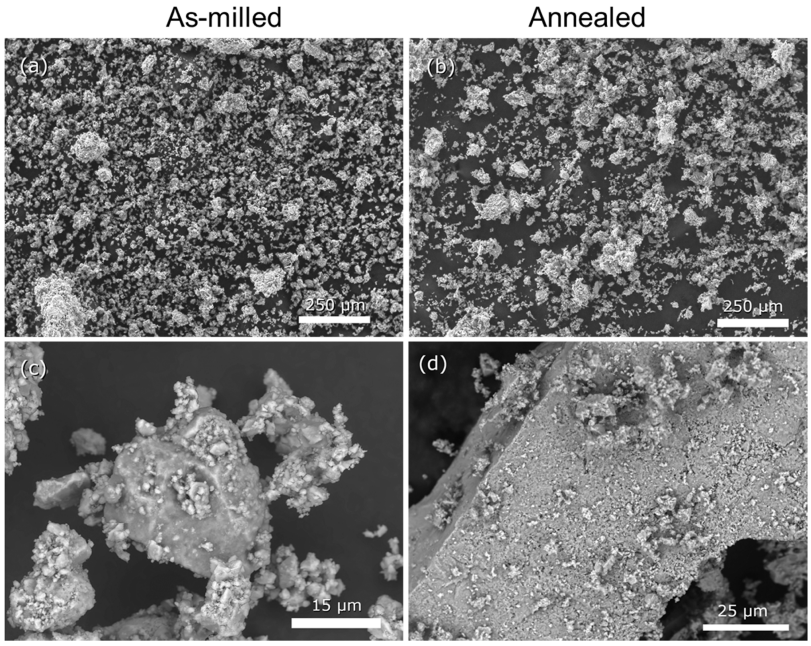

Figure 4. Scanning electron micrographs of as-milled (a) and annealed (b) $NaFeO_2$ in secondary electron imaging show larger particles present for the annealed samples. Backscattered electron images of as-milled (c) and annealed (d) $NaFeO_2$ indicate that the particles within each sample have the same composition.

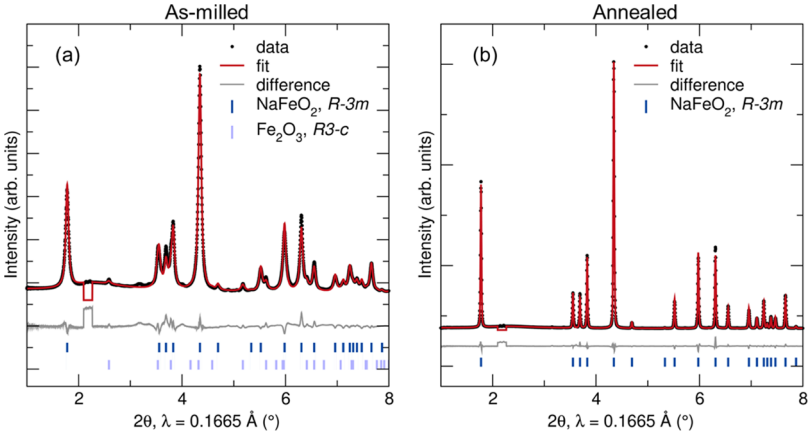

Figure 5. Rietveld refinements of synchrotron XRD data showing the structural differences in (a) as-milled and (b) annealed $NaFeO_2$. The XRD pattern for the as-milled sample has more impurity peaks and broader peaks, indicating a lower crystallinity than observed in the annealed sample.

Since higher temperatures result in more reducing (i.e., lower μ_O) environments, this observation supports the predicted stability of the β phase at lower oxygen chemical potentials in Figure 3.

Defect-dependent stability phase diagrams, such as Figure 3, can be used to both rationalize the appearance of a metastable phase under certain synthesis conditions and as a tool for designing synthesis routes that target a specific phase. In this case, the proximity of the α-$NaFeO_2$ region (red) to the binary phases Na_2O_2 (or NaO_2) and Fe_2O_3 suggests that these phases would be optimal precursors for targeting the α-phase. The shared phase boundary between α-$NaFeO_2$ and O_2 also suggests that an oxygen-rich environment would be the most suitable for synthesis of the α phase. These predictions are supported by our mechanochemical synthesis approach, which directly uses or involves Na_2O_2, Fe_2O_3, and O_2 gases.

3.3. Comparison of As-Milled and Annealed Samples.

The as-milled samples were annealed to increase crystallinity, to further react any remaining γ-Fe_2O_3 and Na_2O_2, and to study changes in material performance because of heat treatment. Upon annealing at 700 °C for 12 h, an increase in the particle size of the samples was observed by scanning electron microscopy (SEM). The as-milled sample, Figure 4a,c, contains both small particles (<5 μm) and larger faceted particles (~30 μm), while the annealed sample, Figure 4b,d, contains larger consolidated particles (>50 μm) and fewer small particles. Images obtained in backscattering mode, Figure 4c,d, show that the particles are relatively uniform in composition throughout the sample.

The stoichiometry of the samples was investigated by inductively coupled plasma−optical emission spectroscopy (ICP-OES). ICP-OES measurements showed that the annealed sample has a lower Na/Fe ratio. The observed Na/Fe ratio for the as-milled sample was 1.03:1, while the annealed sample was 0.94:1, with an error of ±0.006 for the Na measurement and ±0.01 for the Fe measurement. TGA

https://doi.org/10.1021/acs.inorgchem.2c03286
Inorg. Chem. XXXX, XXX, XXX−XXX

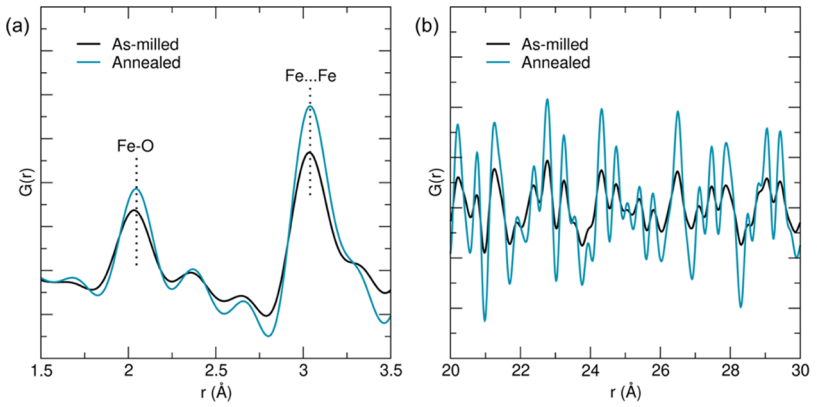

Figure 6. Representative PDF data of annealed (light blue) and as-milled $NaFeO_2$ (black) samples. Dashed vertical lines (a) show that the Fe−O and Fe···Fe distances shift slightly because of the annealing process. The high r data (b) shows sharpening of the peaks in the annealed sample.

measurements of the as-milled sample shown in Figure S7 indicate that there is a mass loss upon heating, which most likely corresponds to a removal of a Na carbonate-terminated particle surface rather than a loss of Na within the bulk of the particles. Therefore, the overall Na/Fe ratio of the samples remains consistent during the annealing process.

The X-ray powder diffraction data for the as-milled and annealed samples showed diffraction peaks that were largely consistent with the reported R-3m model for α-$NaFeO_2$.[72] Parameters from Rietveld refinement of the structural model are reported in Table S1. The peaks for the annealed sample were sharper than those for the as-milled sample, indicating an increase in long-range ordering. Some additional peaks were observed at 2.1, 2.2, 2.7, 3.1, and 3.6° that are consistent with β-$NaFeO_2$ (Figure 5).

The PDFs for the as-milled and annealed samples showed peaks to high r, with largely similar features (see Figure S6). For the annealed sample, the peak corresponding to the Fe−O bond was shifted from 2.037(11) Å in the as-milled sample to 2.049(11) Å in the annealed sample and the peaks at high r were sharper, indicating increased structural ordering relative to the as-milled sample, as shown in Figure 6.

For both samples, the known R-3m model for α-$NaFeO_2$ could effectively fit the experimental PDF data over a short range up to ∼20 Å by including interlayer disorder (Figure S8 and Table S3). Other models with the same FeO_2 layer structure but with different orderings of the stacking were tested against the data. The PDF data, shown in Figure S9, were well fit over an extended range ($R_{annealed}$ ∼ 0.21 $R_{as\text{-}milled}$∼ 0.22, 1.55−20.0 Å) by $C2/m$ that was reported for an α-$NaFeO_2$-type honeycomb with the composition $Na_3Ni_2BiO_6$.[72] The layers in the R-3m α-$NaFeO_2$ structure are comprised of octahedrally coordinated Na atoms, which repeat every three layers ("O3"), while the $C2/m$ $NaFeO_2$ model can be described as having "O2" packing, where the octahedrally coordinated Na atoms repeat every two layers instead of three. There are ∼3.5 layers of FeO octahedra in 20 Å. The refined structural parameters are reported in Table S2.

The Fe−O bond lengths in the as-milled and annealed samples were quantified by fitting Gaussian functions to the peaks in the PDF data. The average Fe−O distance increased from the as-milled sample to the annealed sample, suggesting a possible partial reduction in the average Fe-oxidation state. To investigate the Fe-oxidation state of the samples, Mössbauer spectroscopy was performed on both as-milled and annealed samples. Mössbauer spectra from the as-milled and annealed samples, as shown in Figure 7, suggest no significant reduction of the material (i.e., the iron is trivalent).

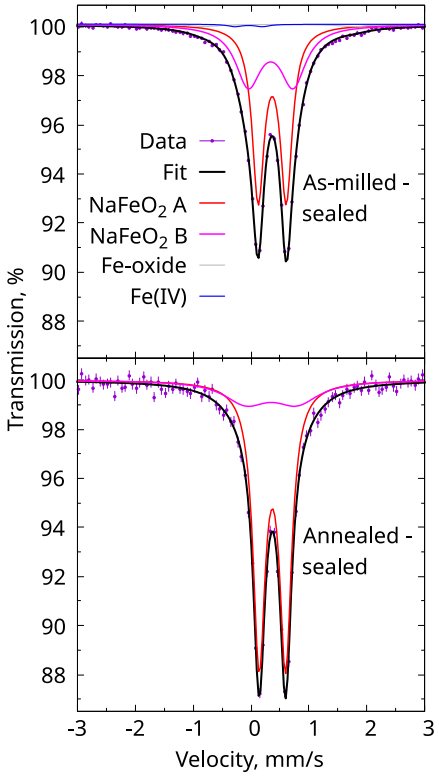

Figure 7. Mössbauer spectroscopy of as-milled and annealed $NaFeO_2$ at 295 K.

The Mössbauer spectra of all samples exhibit a rather narrow Fe(III) doublet with the spectral parameters of $NaFeO_2$ as the majority component, denoted as $NaFeO_2$ A. However, secondary components are required to achieve good fits to the data. For all samples, a second broader doublet with larger quadrupole splitting but a similar isomer shift, $NaFeO_2$ B, is required in the model. Further minor components with constrained spectral parameters were added to the model to check for the presence of iron oxides (hematite and magnetite) and for potential Fe(IV). The spectra and fits for the sealed samples are shown in the central velocity region in Figure 7. The spectrum in the full velocity range, the spectra for the

https://doi.org/10.1021/acs.inorgchem.2c03286
Inorg. Chem. XXXX, XXX, XXX−XXX

samples exposed to ambient conditions, and the detailed spectral parameters and fit procedures are shown in Section S8.

The principal component in all Mössbauer spectra, $NaFeO_2$ A, exhibits an isomer shift of ∼0.36 mm/s and quadrupole splitting of 0.46 mm/s. These parameters are in excellent agreement with recent reports.[44,73,74] The second broader component $NaFeO_2$ B has a slightly smaller isomer shift, ∼0.34 mm/s, and larger quadrupole splitting of ∼0.8 mm/s; this component is also significantly broader, indicating the disorder or distribution of the local environment. A similar increase in quadrupole splitting for part of Fe(III) is observed in *operando* measurements and is typically accompanied by the appearance of Fe(IV)[44,73,74] but is also observed before the appearance of Fe(IV) at $V < 3.8$ V vs Li/Li^+ in $Li(Ni,Fe,Al)O_2$.[75] The likely origin of the B component is thus vacancies nearby the Fe site. Upon annealing, both for the sealed and the ambient condition sample, the relative amount of the B component is reduced from ∼35 to ∼20%, supporting the local disorder as the origin of the larger quadrupole. Furthermore, the annealing process also leads to a reduction of residual iron oxides from about 9% to below the ∼1% detection limit. Finally, minor amounts of Fe(IV) are detected close to the detection limit (0.8%), except in the as-milled samples aged in an ambient atmosphere, where 3% of Fe(IV) is needed to properly fit the data. This could be related to a transient state related to the loss of Na because the long-term stability of Fe(IV) is doubtful under ambient conditions. Overall, Mössbauer spectroscopy indicates that the annealed samples yield rather high-quality and well-crystallized $NaFeO_2$, with about 20% of iron remaining in distorted local coordination after annealing.

The effect of annealing on the electrochemical performance of α-$NaFeO_2$ was investigated through electrochemical cycling, as shown in Figure 8. The as-milled samples show very little capacity (18 mAh/g) on the first cycle that fades quickly. In contrast, the annealed sample shows an activation transition at 3.6 V vs Na/Na^+ for the first cycle with a capacity of 155 mAh/g. The capacity then fades on subsequent cycles due to the degradation of the electrode at voltages above 3.5 V, which has been shown in previous studies to be caused by an irreversible structural change when extracting sodium from the structure.[38,44,45] The activation process observed at 3.6 V indicates that there is a defect structure present in the as-cast material that is hindering further cycling. It is only once the structure is eliminated that the voltage decreases to 3.5 V and cycling continues. This activation process may be accessible in the annealed sample due to the reduction in the disordered component that was observed in the Mössbauer spectra upon annealing of the sample, however, further *operando* cycling would be needed to better understand this activation process.

4. CONCLUSIONS

This paper presents the mechanochemical synthesis of α-$NaFeO_2$. α-$NaFeO_2$ is synthesized directly during the mechanochemical process without any required additional heating of the sample, which is required by other synthesis methods. The synthesis of α-$NaFeO_2$ is shown to be sensitive to the Fe_2O_3 polymorph as well as the mass of the precursor being milled, indicating that the defect concentration and synthesis environment may be critical parameters to gain polymorph control in this system. While the α-phase is predicted by density functional theory calculations to be metastable (even at $T = 0$ K), we show via charged point defect calculations that at high oxygen chemical potentials, α-$NaFeO_2$ is thermodynamically stabilized over the β- and γ-polymorphs due to its greater ability to accommodate equilibrium cation vacancy concentrations at the annealing temperature. Upon annealing the sample, α-$NaFeO_2$ has higher crystallinity, larger particle size, and is less disordered. While the samples are similar in composition, these changes upon annealing lead to improved capacity during electrochemical cycling as the sample goes through an activation process that enables the cycling of the electrode. Mössbauer spectroscopy reveals that after annealing, the phase formed through direct mechanochemical synthesis features trivalent iron and spectral parameters of $NaFeO_2$. The presence of a second broader doublet indicates that about 20% of Fe is in a somewhat deformed environment related to residual defects. Understanding the synthesis process provides important information that may guide further polymorph control in layered transition metal oxides. Also, by studying the structure upon annealing, the role that defects and disorder play on the performance of the final material in electrochemical and other future applications can be better understood.

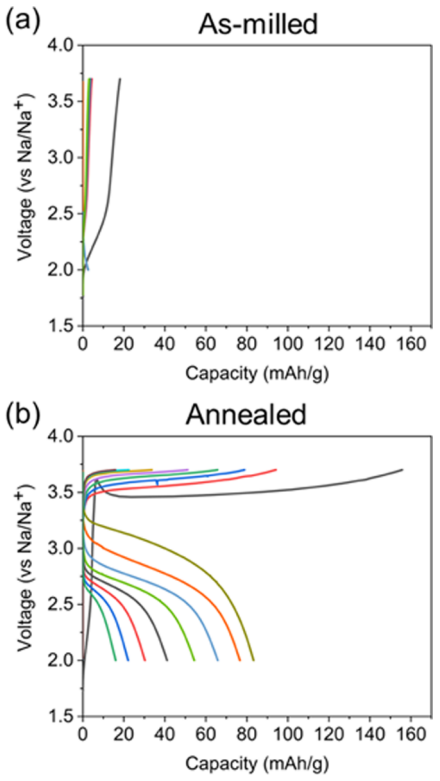

Figure 8. Representative cycling data for (a) as-milled $NaFeO_2$ and (b) annealed $NaFeO_2$. The as-milled sample shows limited cycling, while the annealed sample shows a capacity of 155 mAh/g after an activation transition at 3.6 V. The first cycle (black line) for each sample has the highest capacity, which fades over subsequent cycles.

■ ASSOCIATED CONTENT

Supporting Information

The Supporting Information is available free of charge at https://pubs.acs.org/doi/10.1021/acs.inorgchem.2c03286.

Additional synthesis information; laboratory X-ray diffraction data; magnetic orderings; defect concentrations; Gibbs free-energy curves; thermogravimetric analysis data; analysis parameters from Rietveld refinements; PDF; and Mössbauer analysis (PDF)

https://doi.org/10.1021/acs.inorgchem.2c03286
Inorg. Chem. XXXX, XXX, XXX−XXX

AUTHOR INFORMATION

Corresponding Author

Gabriel M. Veith − *Chemical Sciences Division, Oak Ridge National Laboratory, Oak Ridge, Tennessee 37831, United States;* orcid.org/0000-0002-5186-4461; Email: veithgm@ornl.gov

Authors

Rebecca D. McAuliffe − *Chemical Sciences Division, Oak Ridge National Laboratory, Oak Ridge, Tennessee 37831, United States;* orcid.org/0000-0002-6497-4360

Gabrielle E. Kamm − *Department of Chemistry, Stony Brook University, Stony Brook, New York 11794, United States;* orcid.org/0000-0001-5149-6526

Matthew J. McDermott − *Materials Sciences Division, Lawrence Berkeley National Laboratory, Berkeley, California 94720, United States; Department of Materials Science and Engineering, University of California, Berkeley, Berkeley, California 94720, United States;* orcid.org/0000-0002-4071-3000

Raphaël P. Hermann − *Materials Science and Technology Division, Oak Ridge National Laboratory, Oak Ridge, Tennessee 37831, United States;* orcid.org/0000-0002-6138-5624

Neyanel Vasquez-Garcia − *Chemical Sciences Division, Oak Ridge National Laboratory, Oak Ridge, Tennessee 37831, United States*

Robert L. Sacci − *Chemical Sciences Division, Oak Ridge National Laboratory, Oak Ridge, Tennessee 37831, United States;* orcid.org/0000-0002-0073-5221

Kristin A. Persson − *Department of Materials Science and Engineering, University of California, Berkeley, Berkeley, California 94720, United States; Molecular Foundry, Lawrence Berkeley National Laboratory, Berkeley, California 94720, United States;* orcid.org/0000-0003-2495-5509

Karena W. Chapman − *Department of Chemistry, Stony Brook University, Stony Brook, New York 11794, United States;* orcid.org/0000-0002-8725-5633

Complete contact information is available at: https://pubs.acs.org/10.1021/acs.inorgchem.2c03286

Author Contributions

R.D.M. synthesized the materials and performed characterization of the materials. N.V.-G. performed initial synthesis studies with G.M.V. G.M.V. prepared electrochemical cells and performed cycling measurements. G.E.K. performed synchrotron experiments and analyzed diffraction data with assistance from K.W.C. M.J.M. performed energy and defect calculations with guidance from K.A.P. R.L.S. assisted with TGA measurements. R.P.H. performed Mössbauer spectroscopy measurements. R.D.M. wrote the manuscript with input from all co-authors.

Notes

The authors declare no competing financial interest.

ACKNOWLEDGMENTS

This work was supported as part of GENESIS: A Next Generation Synthesis Center, an Energy Frontier Research Center funded by the U.S. Department of Energy, Office of Science, Basic Energy Sciences under Award Number DE-SC0019212. The work of G.E.K. was in part supported as a part of QuADS: Quantitative Analysis of Dynamic Structures National Science Foundation Research Traineeship Program, grant number NSF DGE 1922639. TGA measurements were supported by the U.S. Department of Energy, Office of Basic Energy Sciences, Division of Materials Science and Engineering. Research was performed at Oak Ridge National Laboratory (ORNL), managed by UT-Battelle, LLC for the U.S. Department of Energy (DOE) under Contract DE-AC05-00OR22725. This research used resources at the 28-ID-1 beamline of the National Synchrotron Light Source II, a U.S. Department of Energy (DOE) Office of Science User Facility operated for the DOE Office of Science by Brookhaven National Laboratory under Contract No. DE-SC0012704. Calculations performed in this research used resources of the National Energy Research Scientific Computing Center (NERSC) under Award Number BES-ERCAP0020225, a U.S. Department of Energy Office of Science User Facility located at Lawrence Berkeley National Laboratory, operated under Contract No. DE-AC02-05CH11231. Mössbauer spectroscopy was supported by the US DOE Office of Science, Basic Energy Science, Materials Science and Engineering Division. The authors would like to thank Nicholas Winner for helpful discussion regarding the analysis of defect thermodynamics.

REFERENCES

(1) Guilmard, M.; Pouillerie, C.; Crouguennec, L.; Delmas, C. Structural and electrochemical properties of $LiNi_{0.70}Co_{0.15}Al_{0.15}O_2$. *Solid State Ionics* **2003**, *160*, 39−50.

(2) Thomas, M. G. S. R.; David, W. I. F.; Goodenough, J. B.; Groves, P. Synthesis and Structural Characterization of the Normal Spinel $Li[Ni_2]O_4$. *Mater. Res. Bull.* **1985**, *20*, 1137−1146.

(3) Gwon, H.; Kim, S. W.; Park, Y. U.; Hong, J.; Ceder, G.; Jeon, S.; Kang, K. Ion-exchange mechanism of layered transition-metal oxides: case study of $LiNi_{0.5}Mn_{0.5}O_2$. *Inorg. Chem.* **2014**, *53*, 8083−8087.

(4) Kalyani, P.; Kalaiselvi, N.; Renganathan, N. G.; Raghavan, M. Studies on $LiNi_{0.7}Al_{0.3-x}Co_xO_2$ solid solutions as alternative cathode materials for lithium batteries. *Mater. Res. Bull.* **2004**, *39*, 41−54.

(5) Obrovac, M. N.; Mao, O.; Dahn, J. R. Structure and electrochemistry of $LiMO_2$ (M = Ti, Mn, Fe, Co, Ni) prepared by mechanochemical synthesis. *Solid State Ionics* **1998**, *112*, 9−19.

(6) Broussely, M.; Perton, F.; Biensan, P.; Bodet, J. M.; Labat, J.; Lecerf, A.; C, D.; Rougier, A.; Peres, J. P. Li_xNiO_2, a promising cathode for rechargeable lithium batteries. *J. Power Sources* **1995**, *54*, 109−114.

(7) Broussely, M.; Perton, F.; Labat, J.; Staniewicz, R. J.; Romero, A. Li/Li_xNiO_2 and $Li/LiCoO_2$ rechargeable systems: comparative study and performance of practical cells. *J. Power Sources* **1993**, *43*, 43−44.

(8) Mizushima, K.; Jones, P. C.; Wiseman, P. J.; Goodenough, J. B. Li_xCoO_2 ($0 < x < 1$): A New Cathode Material for Batteries of High Energy Density. *Mater. Res. Bull.* **1980**, *15*, 783−789.

(9) Xiang, X.; Zhang, K.; Chen, J. Recent Advances and Prospects of Cathode Materials for Sodium-Ion Batteries. *Adv. Mater.* **2015**, *27*, 5343−5364.

(10) Lamb, J.; Jarvis, K.; Manthiram, A. Molten-Salt Synthesis of O3-Type Layered Oxide Single Crystal Cathodes with Controlled Morphology towards Long-Life Sodium-Ion Batteries. *Small* **2022**, *18*, No. 2106927.
(11) Hasa, I.; Buchholz, D.; Passerini, S.; Hassoun, J. A comparative study of layered transition metal oxide cathodes for application in sodium-ion battery. *ACS Appl. Mater. Interfaces* **2015**, *7*, 5206−5212.
(12) Cabana, J.; Chernova, N. A.; Xiao, J.; Roppolo, M.; Aldi, K. A.; Whittingham, M. S.; Grey, C. P. Study of the Transition Metal Ordering in Layered $Na_xNi_{x/2}Mn_{1-x/2}O_2$ $(2/3 \leq x \leq 1)$ and Consequences of Na/Li Exchange. *Inorg. Chem.* **2013**, *52*, 8540−8550.
(13) Huang, Q.; Xu, S.; Xiao, L.; He, P.; Liu, J.; Yang, Y.; Wang, P.; Huang, B.; Wei, W. Improving the Electrochemical Properties of the Manganese-Based P3 Phase by Multiphasic Intergrowth. *Inorg. Chem.* **2018**, *57*, 15584−15591.
(14) Komaba, S.; Yabuuchi, N.; Nakayama, T.; Ogata, A.; Ishikawa, T.; Nakai, I. Study on the Reversible Electrode Reaction of $Na_{1-x}Ni_{0.5}Mn_{0.5}O_2$ for a Rechargeable Sodium-Ion Battery. *Inorg. Chem.* **2012**, *51*, 6211−6220.
(15) Xiao, B.; Omenya, F.; Reed, D.; Li, X. A glance of the layered transition metal oxide cathodes in sodium and lithium-ion batteries: difference and similarities. *Nanotechnology* **2021**, *32*, No. 422501.
(16) Komaba, S.; Takei, C.; Nakayama, T.; Ogata, A.; Yabuuchi, N. Electrochemical intercalation activity of layered $NaCrO_2$ vs. $LiCrO_2$. *Electrochem. Commun.* **2010**, *12*, 355−358.
(17) Vassilaras, P.; Ma, X.; Li, X.; Ceder, G. Electrochemical Properties of Monoclinic $NaNiO_2$. *J. Electrochem. Soc.* **2013**, *160*, A207−A211.
(18) Rai, A. K.; Anh, L. T.; Gim, J.; Mathew, V.; Kim, J. Electrochemical properties of Na_xCoO_2 (x∼0.71) cathode for rechargeable sodium-ion batteries. *Ceram. Int.* **2014**, *40*, 2411−2417.
(19) Han, M. H.; Gonzalo, E.; Casas-Cabanas, M.; Rojo, T. Structural evolution and electrochemistry of monoclinic $NaNiO_2$ upon the first cycling process. *J. Power Sources* **2014**, *258*, 266−271.
(20) Rougier, A.; Gravereau, P.; Delmas, C. Optimization of the Composition of the $Li_{1-z}Ni_{1+z}O_2$ Electrode Materials: Structural, Magnetic, and Electrochemical Studies. *J. Electrochem. Soc.* **1996**, *143*, 1168−1175.
(21) Ohzuku, T.; Ueda, A.; Nagayama, M. Electrochemistry and Structural Chemistry of $LiNiO_2$ (R-3m) for 4 Volt Secondary Lithium Cells. *J. Electrochem. Soc.* **1993**, *140*, 1862−1870.
(22) Qiu, Z.; Zhang, Y.; Dong, P.; Wang, D.; Xia, S. A ternary oxide precursor with trigonal structure for synthesis of $LiNi_{0.80}Co_{0.15}Al_{0.05}O_2$ cathode material. *J. Solid State Electrochem.* **2017**, *21*, 3037−3046.
(23) Su, D.; Wang, C.; Ahn, H. J.; Wang, G. Single crystalline $Na_{0.7}MnO_2$ nanoplates as cathode materials for sodium-ion batteries with enhanced performance. *Chem. − Eur. J.* **2013**, *19*, 10884−10889.
(24) Kim, Y. Lithium nickel cobalt manganese oxide synthesized using alkali chloride flux: morphology and performance as a cathode material for lithium ion batteries. *ACS Appl. Mater. Interfaces* **2012**, *4*, 2329−2333.
(25) Chen, H.; Grey, C. P. Molten Salt Synthesis and High Rate Performance of the "Desert-Rose" form of $LiCoO_2$. *Adv. Mater.* **2008**, *20*, 2206−2210.
(26) Liu, J.; Hou, M.; Yi, J.; Guo, S.; Wang, C.; Xia, Y. Improving the electrochemical performance of layered lithium-rich transition-metal oxides by controlling the structural defects. *Energy Environ. Sci.* **2014**, *7*, 705−714.
(27) Spahr, M. E.; Novak, P.; Schnyder, B.; Haas, O.; Nesper, R. Characterization of layered lithium nickel manganese oxides synthesized by a novel oxidative coprecipitation method and their electrochemical performance as lithium insertion electrode materials. *J. Electrochem. Soc.* **1998**, *145*, 1113−1121.
(28) Xie, H.; Du, K.; Hu, G.; Duan, J.; Peng, Z.; Zhang, Z.; Cao, Y. Synthesis of $LiNi_{0.8}Co_{0.15}Al_{0.05}O_2$ with 5-sulfosalicylic acid as a chelating agent and its electrochemical properties. *J. Mater. Chem. A* **2015**, *3*, 20236−20243.
(29) He, K.; Ruan, Z.; Teng, X.; Zhu, Y. Facile synthesis and electrochemical properties of spherical $LiNi_{0.85-x}Co_{0.15}Al_xO_2$ with sodium aluminate via co-precipitation. *Mater. Res. Bull.* **2017**, *90*, 131−137.
(30) Seo, J.-S.; Lee, J.-w. Fast growth of the precursor particles of $Li(Ni_{0.8}Co_{0.16}Al_{0.04})O_2$ via a carbonate co-precipitation route and its electrochemical performance. *J. Alloys Compd.* **2017**, *694*, 703−709.
(31) Mohan Rao, M.; Jayalakshmi, M.; Schaf, O.; Guth, U.; Wulff, H.; Scholz, F. Electrochemical behaviour of solid lithium nickelate ($LiNiO_2$) in an aqueous electrolyte system. *J. Solid State Electrochem.* **1999**, *4*, 17−23.
(32) Kalyani, P.; Kalaiselvi, N.; Muniyandi, N. A new solution combustion route to synthesize $LiCoO_2$ and $LiMn_2O_4$. *J. Power Sources* **2002**, *111*, 232−238.
(33) Kwon, S. N.; Song, J.; Mumm, D. R. Effects of cathode fabrication conditions and cycling on the electrochemical performance of $LiNiO_2$ synthesized by combustion and calcination. *Ceram. Int.* **2011**, *37*, 1543−1548.
(34) Purwanto, A.; Yudha, C. S.; Ubaidillah, U.; Widiyandari, H.; Ogi, T.; Haerudin, H. NCA cathode material: synthesis methods and performance enhancement efforts. *Mater. Res. Express* **2018**, *5*, No. 122001.
(35) Mao, F.; Guo, W.; Ma, J. Research progress on design strategies, synthesis and performance of $LiMn_2O_4$-based cathodes. *RSC Adv.* **2015**, *5*, 105248−105258.
(36) Fergus, J. W. Recent developments in cathode materials for lithium ion batteries. *J. Power Sources* **2010**, *195*, 939−954.
(37) Okada, S.; Takahashi, Y.; Kiyabu, T.; Doi, T.; Yamaki, J.-I.; Nishida, T. Layered Transition Metal Oxides as Cathodes for Sodium Secondary Battery. *ECS Meet. Abstr.* **2006**, *MA2006-02*, 201.
(38) Yabuuchi, N.; Yoshida, H.; Komaba, S. Crystal Structures and Electrode Performance of Alpha-$NaFeO_2$ for Rechargeable Sodium Batteries. *Electrochemistry* **2012**, *80*, 716−719.
(39) Kubota, K.; Asari, T.; Yoshida, H.; Yaabuuchi, N.; Shiiba, H.; Nakayama, M.; Komaba, S. Understanding the Structural Evolution and Redox Mechanism of a $NaFeO_2$-$NaCoO_2$ Solid Solution for Sodium-Ion Batteries. *Adv. Funct. Mater.* **2016**, *26*, 6047−6059.
(40) Yoshida, H.; Yabuuchi, N.; Komaba, S. Na Insertion Mechanism in Alpha $NaFeO_2$ as Positive Electrode Materials for Na-Ion Batteries. *ECS Meet. Abstr.* **2012**, *MA2012-02*, 1850.
(41) Kugai, J.; Mine, H.; Seino, S.; Nakagawa, T.; Yamamoto, T. A.; Yamada, H. Effects of sodium nitrate and heat treatment atmosphere on the synthesis of α−$NaFeO_2$ layered oxide. *Mater. Chem. Phys.* **2020**, *249*, No. 122948.
(42) Takeda, Y.; Akagi, J.; Edagawa, A.; Inagaki, M.; Naka, S. A Preparation and Polymorphic Relation of Sodium Iron Oxide ($NaFeO_2$). *Mater. Res. Bull.* **1980**, *15*, 1167−1172.
(43) Monyoncho, E.; Bissessur, R. Unique properties of α-$NaFeO_2$: De-intercalation of sodium via hydrolysis and the intercalation of guest molecules into the extract solution. *Mater. Res. Bull.* **2013**, *48*, 2678−2686.
(44) Zhao, J.; Zhao, L.; Dimov, N.; Okada, S.; Nishida, T. Electrochemical and Thermal Properties of α-$NaFeO_2$ Cathode for Na-Ion Batteries. *J. Electrochem. Soc.* **2013**, *160*, A3077−A3081.
(45) Susanto, D.; Cho, M. K.; Ali, G.; Kim, J.-Y.; Chang, H. J.; Kim, H.-S.; Nam, K.-W.; Chung, K. Y. Anionic Redox Activity as a Key Factor in the Performance Degradation of $NaFeO_2$ Cathodes for Sodium Ion Batteries. *Chem. Mater.* **2019**, *31*, 3644−3651.
(46) Kosova, N. V. Mechanochemical Synthesis of Cathode Materials for Lithium Batteries. In *Materials for Lithium-Ion Batteries*; Julien, C.; Stoynov, Z., Eds.; Springer: The Netherlands, 2000; pp 497−500.
(47) Chang, C.-C.; Kumta, P. N. Mechanochemical synthesis of $LiNiO_2$. *Mater. Sci. Eng. B* **2005**, *116*, 341−345.
(48) Choi, H.-J.; Lee, K.-M.; Kim, G.-H.; Lee, J.-G. Mechanochemical Synthesis and Electrochemical Properties of $LiMn_2O_4$. *J. Am. Ceram. Soc.* **2001**, *84*, 242−244.

https://doi.org/10.1021/acs.inorgchem.2c03286
Inorg. Chem. XXXX, XXX, XXX−XXX

(49) Kononova, O.; Huo, H.; He, T.; Rong, Z.; Botari, T.; Sun, W.; Tshitoyan, V.; Ceder, G. Text-mined dataset of inorganic materials synthesis recipes. *Sci. Data* **2019**, *6*, 203.
(50) Toby, B. H.; Von Dreele, R. B. GSAS-II: the genesis of a modern open-source all purpose crystallography software package. *J. Appl. Crystallogr.* **2013**, *46*, 544−549.
(51) Yang, X.; Farrow, C. L.; Billinge, S. J. L.et al.xPDFsuite: an end-to-end software solution for high throughput pair distribution function transformation, visualization and analysis, 2014. https://arxiv.org/abs/1402.3163.
(52) Farrow, C. L.; Juhas, P.; Liu, J. W.; Bryndin, D.; Bozin, E. S.; Bloch, J.; Proffen, T.; Billinge, S. J. PDFfit2 and PDFgui: computer programs for studying nanostructure in crystals. *J. Phys.: Condens. Matter* **2007**, *19*, No. 335219.
(53) Wojdyr, M. Fityk: a general-purpose peak fitting program. *J. Appl. Crystallogr.* **2010**, *43*, 1126−1128.
(54) Momma, K.; Izumi, F. VESTA3 for three-dimensional visualization of crystal, volumetric and morphology data. *J. Appl. Crystallogr.* **2011**, *44*, 1272−1276.
(55) Shenoy, G. K. Mössbauer-Effect Isomer Shifts. In *Mössbauer Spectroscopy Applied to Inorganic Chemistry*; Long, G. J., Ed.; Modern Inorganic Chemistry; Springer, 1984; Vol. *1*.
(56) Hermann, R. P. Mößbauer Spectroscopy. In *Handbook of Solid State Chemistry*; Dronskowski, R.; Kikkawa, S.; Stein, A., Eds.; Wiley-VCH, 2017; Vol. *3*, pp 443−484.
(57) Kresse, G.; Furthmuller, J. Efficient iterative schemes for *ab initio* total-energy calculations using a plane-wave basis set. *Phys. Rev. B* **1996**, *54*, 11169.
(58) Kresse, G.; Joubert, D. From ultrasoft pseudopotentials to the projector augmented-wave method. *Phys. Rev. B* **1999**, *59*, 1758.
(59) Perdew, J. P.; Burke, K.; Ernzerhof, M. Generalized Gradient Approximation Made Simple. *Phys. Rev. Lett.* **1996**, *77*, 3865.
(60) Wang, L.; Maxisch, T.; Ceder, G. Oxidation energies of transition metal oxides within the GGA+*U* framework. *Phys. Rev. B* **2006**, *73*, No. 195107.
(61) Ong, S. P.; Richards, W. D.; Jain, A.; Hautier, G.; Kocher, M.; Cholia, S.; Gunter, D.; Chevrier, V. L.; Persson, K. A.; Ceder, G. Python Materials Genomics (pymatgen): A robust, open-source python library for materials analysis. *Comput. Mater. Sci.* **2013**, *68*, 314−319.
(62) Heyd, J.; Scuseria, G. E.; Ernzerhof, M. Hybrid functionals based on a screened Coulomb potential. *J. Chem. Phys.* **2003**, *118*, 8207−8215.
(63) Jain, A.; Ong, S. P.; Hautier, G.; Chen, W.; Richards, W. D.; Dacek, S.; Cholia, S.; Gunter, D.; Skinner, D.; Ceder, G.; Persson, K. A. Commentary: The Materials Project: A materials genome approach to accelerating materials innovation. *APL Mater.* **2013**, *1*, No. 011002.
(64) Horton, M. K.; Montoya, J. H.; Liu, M.; Persson, K. A. High-throughput prediction of the ground-state collinear magnetic order of inorganic materials using Density Functional Theory. *npj Comput. Mater.* **2019**, *5*, No. 64.
(65) Mathew, K.; Montoya, J. H.; Faghaninia, A.; Dwarakanath, S.; Aykol, M.; Tang, H.; Chu, I.-h.; Smidt, T.; Bocklund, B.; Horton, M.; et al. Atomate: A high-level interface to generate, execute, and analyze computational materials science workflows. *Comput. Mater. Sci.* **2017**, *139*, 140−152.
(66) Freysoldt, C.; Neugebauer, J.; Van de Walle, C. G. Fully *ab initio* finite-size corrections for charged-defect supercell calculations. *Phys. Rev. Lett.* **2009**, *102*, No. 016402.
(67) Broberg, D.; Medasani, B.; Zimmermann, N. E. R.; Yu, G.; Canning, A.; Haranczyk, M.; Asta, M.; Hautier, G. PyCDT: A Python toolkit for modeling point defects in semiconductors and insulators. *Comput. Phys. Commun.* **2018**, *226*, 165−179.
(68) Todd, P. K.; McDermott, M. J.; Rom, C. L.; Corrao, A. A.; Denney, J. J.; Dwaraknath, S. S.; Khalifah, P. G.; Persson, K. A.; Neilson, J. R. Selectivity in Yttrium Manganese Oxide Synthesis via Local Chemical Potentials in Hyperdimensional Phase Space. *J. Am. Chem. Soc.* **2021**, *143*, 15185−15194.
(69) Freysoldt, C.; Grabowski, B.; Hickel, T.; Neugebauer, J.; Kresse, G.; Janotti, A.; Van de Walle, C. G. First-principles calculations for point defects in solids. *Rev. Mod. Phys.* **2014**, *86*, 253−305.
(70) Todd, P. K.; Wustrow, A.; McAuliffe, R. D.; McDermott, M. J.; Tran, G. T.; McBride, B. C.; Boeding, E. D.; O'Nolan, D.; Liu, C. H.; Dwaraknath, S. S.; et al. Defect-Accommodating Intermediates Yield Selective Low-Temperature Synthesis of $YMnO_3$ Polymorphs. *Inorg. Chem.* **2020**, *59*, 13639−13650.
(71) West, A. R. $NaAlO_2$ and $NaFeO_2$ Polymorphism. *Nature* **1974**, *249*, 245−246.
(72) Seibel, E. M.; Roudebush, J. H.; Wu, H.; Huang, Q.; Ali, M. N.; Ji, H.; Cava, R. J. Structure and magnetic properties of the alpha-$NaFeO_2$-type honeycomb compound $Na_3Ni_2BiO_6$. *Inorg. Chem.* **2013**, *52*, 13605−13611.
(73) Fehse, M.; Bessas, D.; Mahmoud, A.; Diatta, A.; Hermann, R. P.; Stievano, L.; Sougrati, M. T. The Fe 4+/3+ Redox Mechanism in $NaFeO_2$: A Simultaneous Operando Nuclear Resonance and X-ray Scattering Study. *Batteries Supercaps* **2020**, *3*, 1341−1349.
(74) Lee, E.; Brown, D. E.; Alp, E. E.; Ren, Y.; Lu, J.; Woo, J.-J.; Johnson, C. S. New Insights into the Performance Degradation of Fe-Based Layered Oxides in Sodium-Ion Batteries: Instability of Fe^{3+}/Fe^{4+} Redox in α-$NaFeO_2$. *Chem. Mater.* **2015**, *27*, 6755−6764.
(75) Muralidharan, N.; Essehli, R.; Hermann, R. P.; Amin, R.; Jafta, C.; Zhang, J.; Liu, J.; Du, Z.; Meyer, H. M., 3rd; Self, E.; et al. Lithium Iron Aluminum Nickelate, $LiNi_xFe_yAl_zO_2$ -New Sustainable Cathodes for Next-Generation Cobalt-Free Li-Ion Batteries. *Adv. Mater.* **2020**, *32*, No. 2002960.

https://doi.org/10.1021/acs.inorgchem.2c03286
Inorg. Chem. XXXX, XXX, XXX−XXX